Measurement of Impulsive Thrust from a Closed Radio Frequency Cavity in Vacuum

Harold White[1], Paul March[2], James Lawrence[3],

Jerry Vera[4], Andre Sylvester[5], David Brady[6], and Paul Bailey[7]
NASA Johnson Space Center, 2101 NASA Parkway, Houston, TX 77058

A vacuum test campaign evaluating the impulsive thrust performance of a tapered RF test article excited in the TM212 mode at 1,937 megahertz (MHz) has been completed. The test campaign consisted of a forward thrust phase and reverse thrust phase at less than 8×10^{-6} Torr vacuum with power scans at 40 watts, 60 watts, and 80 watts. The test campaign included a null thrust test effort to identify any mundane sources of impulsive thrust, however none were identified. Thrust data from forward, reverse, and null suggests that the system is consistently performing with a thrust to power ratio of 1.2 ± 0.1 mN/kW.

---

[1] Advanced Propulsion Theme Lead and Principal Investigator, Eagleworks Laboratories, NASA Johnson Space Center/EP4, Houston, TX, AIAA Member.
[2] Principal Engineer, Eagleworks Laboratories, NASA Johnson Space Center/EP4, Houston, TX, AIAA Senior Member.
[3] Electrical Engineer, Eagleworks Laboratories, NASA Johnson Space Center/EP5, Houston, TX.
[4] Mechanical Engineer and COMSOL Multiphysics Analyst, Eagleworks Laboratories, NASA Johnson Space Center/EP4, Houston, TX.
[5] Project Manager, Eagleworks Laboratories, NASA Johnson Space Center, Houston, TX.
[6] Aerospace Engineer, Eagleworks Laboratories, NASA Johnson Space Center, Houston, TX.
[7] Scientist, Eagleworks Laboratories, NASA Johnson Space Center, Houston, TX.

Nomenclature

$QVPT$	=	Quantum Vacuum Plasma Thruster (a.k.a. Q-thruster)
RF	=	radio frequency
SED	=	Stochastic Electrodynamics
$TM212$	=	Transverse Magnetic 212 Mode
ZPF	=	Zero Point Field
$\vec{F}$	=	force (unit: N)
$\vec{f}$	=	force density (unit: N/m^3)
$\vec{x}$	=	position (unit: m)
$\vec{v}$	=	velocity (unit: m/s)
$\vec{a}$	=	acceleration (unit: m/s^2)
t	=	time (unit: s)
q	=	elementary charge (unit: C)
$\vec{E}$	=	electric field (unit: V/m)
$\vec{B}$	=	magnetic field (unit: T)
ϵ_0	=	vacuum permittivity (unit: F/m)
μ_0	=	vacuum permeability (unit: N/A^2)
h	=	Planck constant (unit: J s)
c	=	vacuum speed of light (unit: m/s)
U	=	electromagnetic energy density (unit: J/m^3)
n_{photon}	=	number density of photons (unit: #/m^3)
ρ_ν	=	vacuum density (unit: kg/m^3)
λ	=	average photon spacing (unit: m)
f	=	frequency (unit: Hz)

I.   Introduction

It has been previously reported that RF resonant cavities have generated anomalous thrust on a low thrust torsion pendulum [1, 2] in spite of the *apparent* lack of a propellant or other medium with which to exchange momentum. It is shown here that a dielectrically loaded tapered RF test article excited in the TM212 mode (see Figure 1) at 1,937 MHz is capable of consistently generating force at a thrust to power level of 1.2 ± 0.1 mN/kW with the force directed to the narrow end under vacuum conditions.
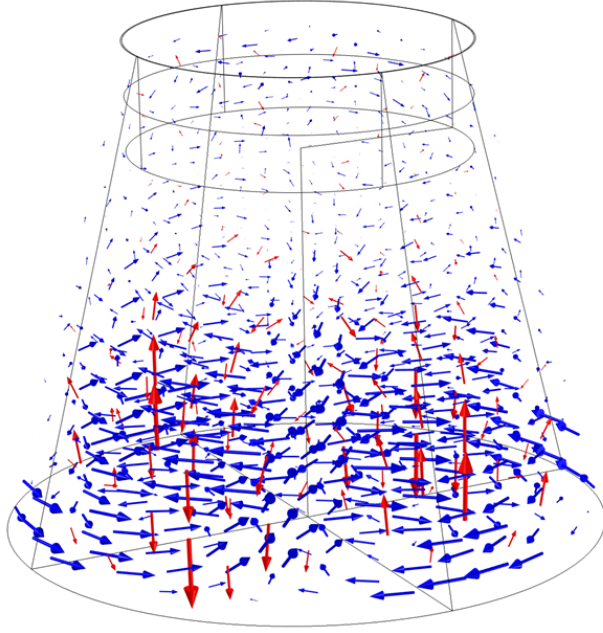
Fig. 1: TM212 field lines in dielectric loaded cavity, red arrows represent electric field, blue arrows represent magnetic field.

II. Experimentation

A. Facilities

The thrust measurements were made using the low-thrust torsion pendulum at NASA's Johnson Space Center (JSC). This torsion pendulum is capable of measuring thrust down to the single-digit μN level. Figure 2 shows a simple representation of the torsion pendulum's major elements. The torsion pendulum is constructed primarily of aluminum structure that is mounted on a slide-out table within a 0.762 m by 0.914 m vacuum chamber. The chamber is subsequently mounted on a 1.219 m by 2.438 m optical bench. The pendulum arm pivots about two linear flexure bearings in a plane normal to gravitational acceleration. For every thrust measurement, a calibration force is provided by means of establishing a voltage potential across a set of interleaving aluminum electrostatic fins [3], with one set of fins on the fixed structure and one set on the pendulum arm. The fins overlap without touching. A calibration voltage is applied to the fixed structure fins, which induces a force upon the pendulum arm fins and an associated displacement that is measured by the system. The electrostatic fins design provides a constant electrostatic force over a reasonably

large range (between 30-70% overlap, or a few mm of travel), so adjustments to the calibration mechanism between test run data takes is usually not required. Calibration of the overlap/force relationship was accomplished using a Scientech SA 210 precision weighing balance (resolution to one μN). The displacement of the torsion pendulum is recorded by an optical displacement sensor, and the steady state displacement from the calibration force is used to calibrate any force applied to the torsion pendulum by a device under test. The optical displacement sensor can be accurately positioned relative to the torsion pendulum by means of X-Y-Z micro-positioning stages. Whenever a force is induced upon the pendulum arm, the resultant harmonic motion must be damped. This is accomplished via the use of a magnetic damper at the back of the torsion pendulum arm. Four Neodymium (NdFeB Grade N42) block magnets interact with the pendulum's copper damper angle bracket to dampen oscillatory motion. The magnets are housed in a low-carbon steel square tube to better localize the magnetic field of the magnets in the damper and not in the chamber. Vacuum conditions are provided by two roughing pumps and two high-speed turbo pumps, and all vacuum tests were performed at or below 8×10^{-6} Torr. The high-frequency vibrations from the turbo pump have no noticeable effect on the testing seismic environment.

All DC power and control signals pass between the external equipment and vacuum chamber internal components via sealed feed through ports. Inside the vacuum chamber, all DC power and control signals that pass between the torsion pendulum fixed structure and the pendulum arm are transmitted via liquid metal contacts in order to eliminate interface cable forces. Each liquid metal contact consists of a physical but non-force-producing interface between a brass screw and a small socket filled with Galinstan$^{\text{TM}}$ liquid metal. The test article is mounted on the end of the pendulum arm closest to the chamber door. Test article support electronics - e.g., signal generators, amplifiers, phase adjusters - may be mounted on either end of the pendulum arm. If needed, ballast is added to the pendulum arm to eliminate moments that affect the neutral position of the pendulum arm. After a test article is mounted on the pendulum arm, a typical test run data take consists of a pre-run calibration (using the electrostatic fin mechanism), followed by energizing the test article, and finishing with a post-run calibration and data recording.
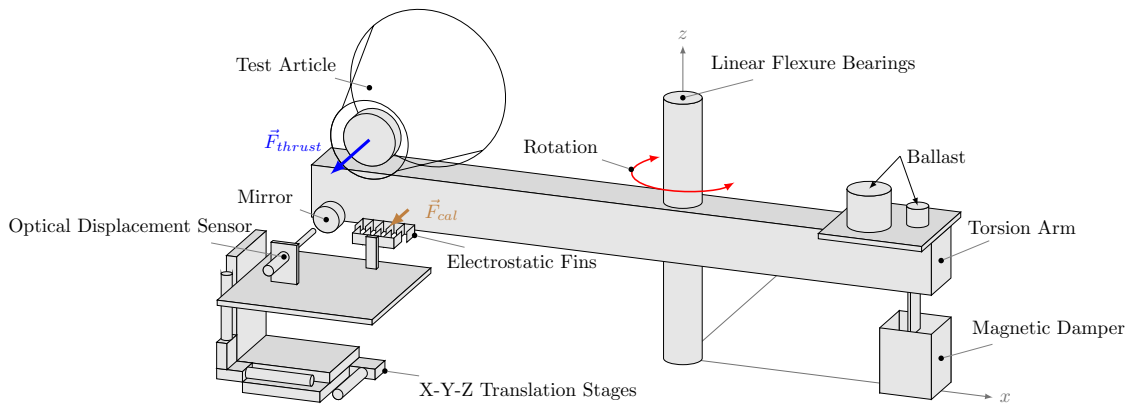
Fig. 2: Simplified Representation of Torsion Pendulum.

B. Test Article

The RF resonance test article is a copper frustum with an inner diameter of 27.9 cm on the big end, inner diameter of 15.9 cm on the small end, and an axial length of 22.9 cm. The test article contains a 5.4 cm-thick disc of polyethylene with an outer diameter of 15.6 cm that is mounted to the inside face of the smaller diameter end of the frustum. A 13.5 millimeter diameter loop antenna drives the system in the TM212 mode at 1,937 MHz. Because there are no analytical solutions for the resonant modes of a truncated cone, the use of the term TM212 describes a mode with two nodes in the axial direction, and four nodes in the azimuthal direction. A small whip antenna provides feedback to the Phase Locked Loop (PLL) system. Figure 3 provides a block diagram of the test article's major elements.

The loop antenna is driven by an RF amplifier that is mounted on the torsion arm with the test article. The signal from the RF amplifier is routed to the test article's loop antenna through a dual directional coupler and a three stub tuner. The dual directional coupler is used to measure the power forward to the test article, and the power reflected from the test article. The three stub tuner is used as a matching network to create a 50Ω load as seen by the RF amplifier at the target drive frequency. In an ideally-tuned RF resonance system, the power forward would be maximized while the power reflected would be minimized using some form of control logic, be it manual or automatic tuning. The RF amplifier gets the input signal to be amplified from the PLL circuit. The PLL circuit is in essence the control electronics that reads the "echo" (AC electric field signal at actual
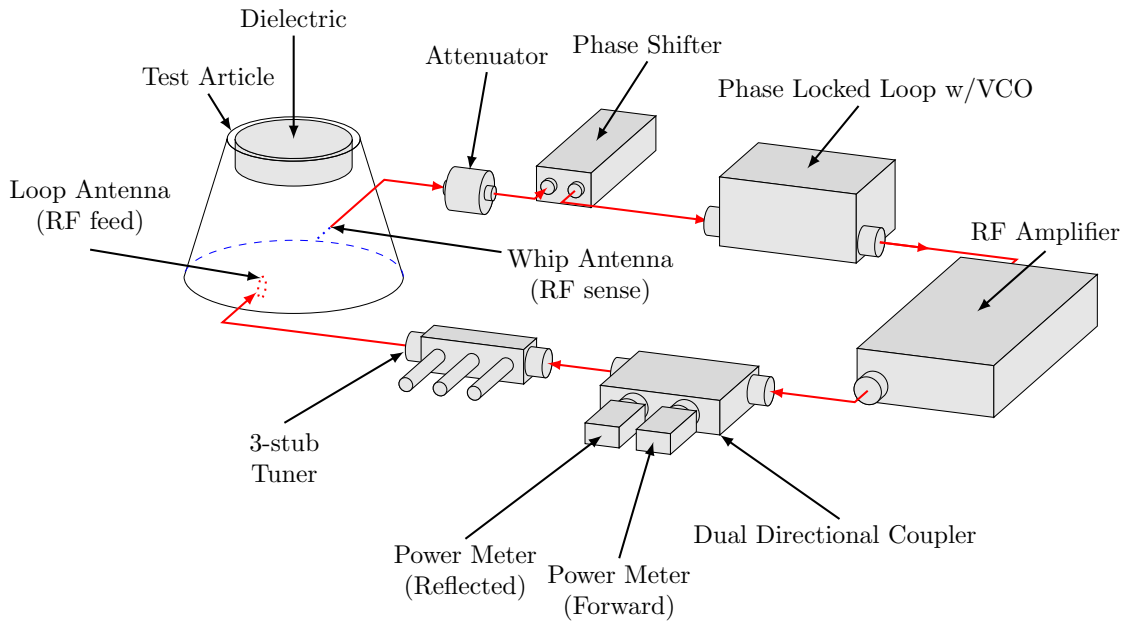
5

Fig. 3: Block Diagram of Integrated Tapered Test Article: All components depicted are kitted together into an integrated test article that is mounted to the end of the torsion arm.

resonance frequency) from the RF resonance system by means of the whip antenna, compares the "echo" to the drive signal using a mixer, determines the appropriate DC drive voltage for the Voltage Controlled Oscillator (VCO) to ensure that the drive signal is properly matched to the "echo" in the system and keeps the system on resonance even though components get warmer and geometry changes slightly due to thermal expansion shifting the resonance. All of the elements depicted in Figure 3 are assembled into an integrated test article that is represented as the large conical object labeled "Test Article" in Figure 2.

Not shown in the block diagram for clarity are the signals from the control panel and instrumentation outside of the vacuum chamber. The "seed" frequency for the voltage controlled oscillator located in the PLL box is determined by an external control voltage. In a sense, this provides the PLL with a "starting" frequency to then delta away from as necessary to keep the system in optimal resonance conditions within the bandwidth of the PLL. In this way, the test article can be resonated in any chosen RF resonance modes by setting this "seed" frequency close to a known resonance, and the system will "snap" onto and maintain resonance at the target mode. The power magnitude is established by providing a control voltage to a Variable Voltage Attenuator (VVA) that attenuates

the output from the VCO that is then routed to the RF amplifier for amplification. The power forward and power reflected meters provide a DC signal proportional to the power reading, and are routed to the lab data acquisition rack for conversion and display to the operator.

1. *Optimal Tuning*

Considerable time and effort was spent empirically studying and mapping out the optimal and non-optimal RF tuning configurations for the TM212 mode to generate maximum thrust. One impetus for this effort was earlier observations in the lab that showed one could have an optimally tuned RF resonance system that could generate a large amount of thrust in one set of RF tuning conditions, and generate a small amount of thrust in another set of RF tuning conditions. In both cases, the system was an effectively tuned RF resonance system with high quality factor and low reflected power at run-time. The other impetus for this effort was that the model used to predict thrust performance for a given RF resonance mode, test article geometry, and dielectric loading showed that the force magnitude was highly non-linear as a function of input power suggesting that RF tuning for maximum thrust will have tighter constraints than just RF tuning for optimal RF resonance. A VCO, even though it is effectively a mono-sinusoidal source, still has some frequency jitter about the frequency set point. This jitter in practice can reduce the effective thrust as the system spends a small fraction of time at a slightly non-optimal thrust configuration with a periodicity linked to the VCO's frequency jitter. Also, the PLL may add some small offsets to the "locked" frequency center point.

For the process of conducting this highly empirical system study, each tuning iteration would establish an RF tuning and operational condition for the integrated system. An Agilent Technologies Field Fox Vector Network Analyzer (VNA)(N9923A) was used to quantify the RF characteristics for the established resonance. The Smith chart for the system was used for initial tuning using the three-stub tuner, choice of loop antenna, and orientation of the loop antenna relative to the test article. The loaded quality factor was calculated for each RF tuning configuration to be tested. The change in phase angle over frequency would also be calculated, and a new parameter dubbed phase angle quality factor was developed to help quantify the characteristics of a given resonance

condition. The phase angle quality factor is the change in phase angle over a given frequency range, and was determined using the phase plot from the VNA and only considering the region of steepest phase angle change centered on the resonance. Figure 4 depicts a montage of plots from the VNA for a given set point. In the figure, the top left pane is the log S11 plot that is used to calculate the loaded quality factor and any asymmetry to the RF resonance (upper side band compared to lower side band). The top right pane is the Smith chart for the system, and the nomenclature "-j65" represents the angle of line through the center of the system's circle as it corresponds to complex impedance on the perimeter of the Smith chart. The bottom left pane is the variation in phase angle for the system, and the bottom right is the group delay.

The tuning study determined for this particular tapered test article that optimal thrust was present if the system had a quality factor of at least several thousand and the maximum phase angle quality factor that could be achieved. In practice, this latter metric means the system is usually just slightly over-coupled, and the circle in the top right pane of the figure will just encircle the center of the Smith chart (50Ω point).

C.   Vacuum Campaign

1.   Signal Superposition

Figure 5 shows a conceptual simulation of the superposition of an impulsive signal and a thermal signal (from thermal expansion of the system). The simulation is a simple mathematical representation of the combination of a signal with steady state magnitude, quick rise/fall times (impulsive content); and a logarithmic signal that increases while the impulsive signal is present and decreases when the impulsive signal is removed (thermal content). This figure shows a scenario where the magnitudes of the impulsive and thermal are similar, and the polarities are the same. Inspecting the plot, one can see that the thermal signal creates a shifting baseline for the impulse-signal. The evidence for the presence of the impulsive signal is the strong discontinuity of slope on the leading edge of the superposition trace. The relative magnitude of the impulsive signal can be determined by taking the lay or path of the superposition trace after this discontinuity, and shifting it down so that the projection of this curve would intersect with the origin. This approximately detangles the

8

(a) Return Loss

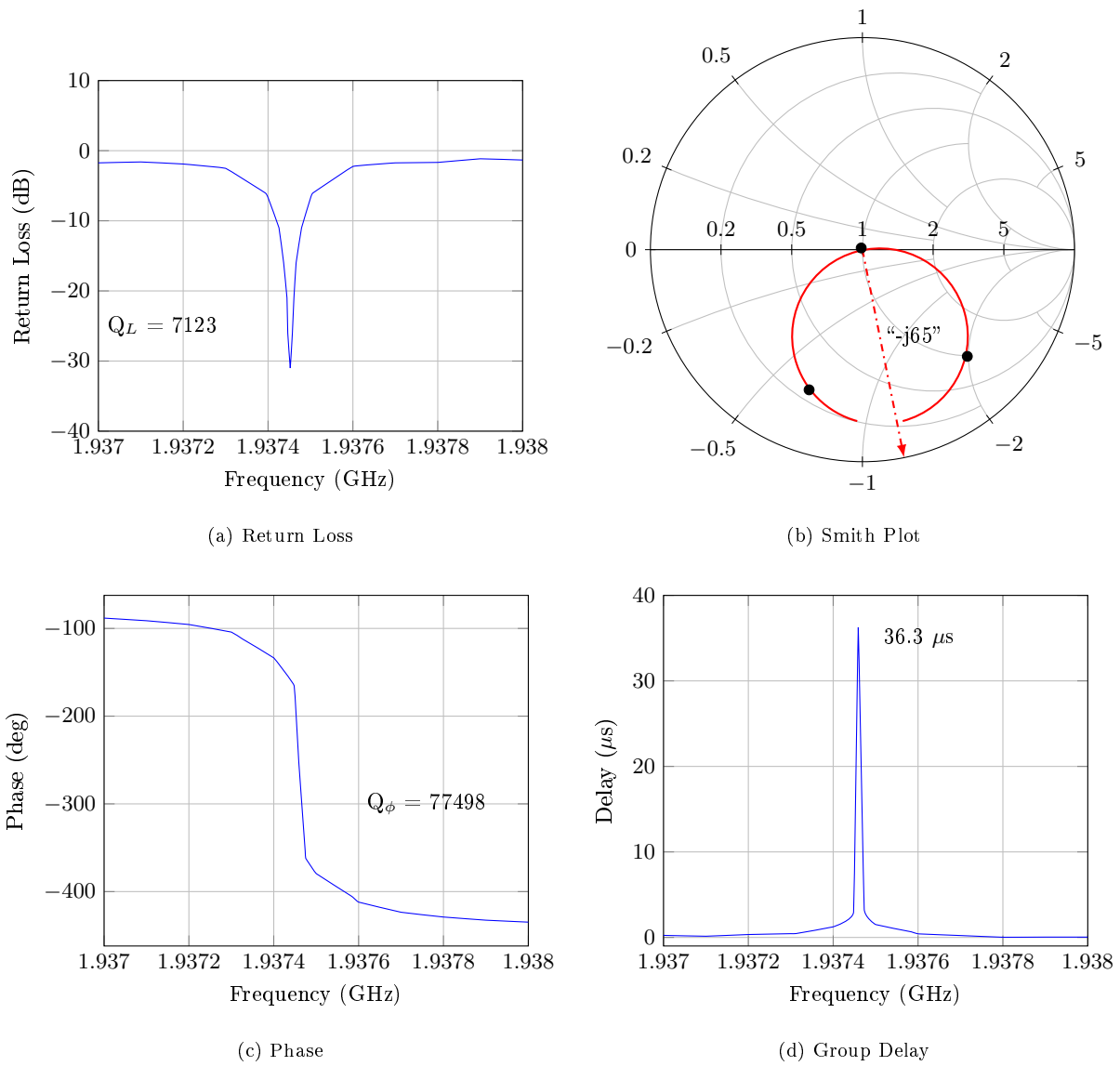(b) Smith Plot

(c) Phase

(d) Group Delay

Fig. 4: Data for a given RF configuration collected using an Agilent Technologies N9923A(4GHz) Field Fox RF Vector Network Analyzer.

Panel (a) shows the return loss as a function of frequency and is used to calculate the quality factor. The dip in the plot denotes the resonance frequency. Panel (b) shows the Smith Chart for the integrated test article and is used as a tuning guide. Panel (c) shows the change in phase as the system moves through the resonance and is used to calculate a phase quality factor. Panel (d) shows the Group Delay which is an alternative way to see the resonance and quality of the RF system.

impulsive thrust part from the thermal part. As can be seen from the plot, when the impulsive signal is terminated, the discontinuity of slope in the superposition trace can be very subtle depending on the magnitude of the impulsive signal to the thermal signal. In this simulation case, the trailing edge discontinuity is not detectable, while the leading edge is clearly detectable.
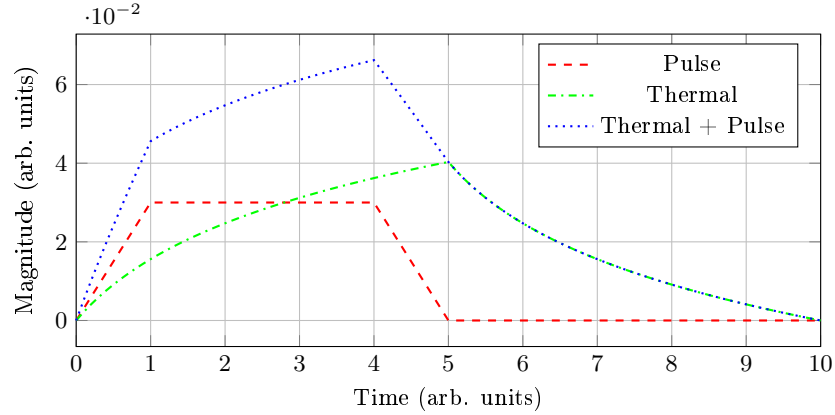

Fig. 5: Superposition of Signals: Conceptual superposition of an impulsive thrust (red) and thermal drift (green) signal over an on/off power cycle on the torsion pendulum.

The nature of the optical displacement signals collected during testing activities conducted under atmospheric conditions showed that the impulsive signal was much larger than the thermal signal, likely due to convection cooling precluding heat buildup. Testing under vacuum conditions showed an increase in thermal drift compared to atmospheric runs due to radiative cooling limitations, while the impulsive signal stays the same. As a result, the thermal signal in the vacuum runs is slightly larger than the magnitude of the impulsive signal. Detailed thermal testing and analysis of the test article in air and under vacuum showed that the aluminum heat sink is the dominant contributor to the thermal signal. Figure 6 shows thermal imagery of the test article after a run and the aluminum heat sink is the hottest surface in the post-test imagery. As the aluminum heat sink gets warmer, its thermal expansion dominates the shifting center of gravity (CG) of the test article mounted on the torsion pendulum. This CG shift causes the balanced neutral point baseline of the torsion pendulum to shift with the same polarity as the impulsive signal when the test article is mounted in the forward or reverse thrust directions. Figure 7 shows a forward thrust run in vacuum conditions of the tapered test article operated in the targeted TM212 mode with an input power of ∼60 W.

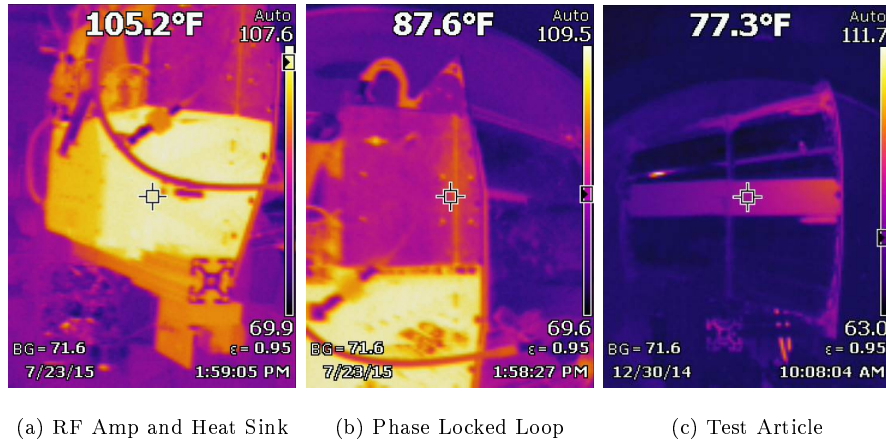(a) RF Amp and Heat Sink   (b) Phase Locked Loop   (c) Test Article

Fig. 6: IR Imagery of Test Article After Testing: Left pane shows RF Amp and heat sink; middle pane shows phase locked loop; right pane shows copper test article. Imagery was taken by a Fluke Ti100 Thermal Imager.

The characteristic discontinuity of slope is evident on the leading edge of the superposition trace from the optical displacement sensor. The characteristics of the curve after this discontinuity are used as the baseline to be shifted down so that the line projects back to the "origin" or moment when RF power was activated. This is the technique used to assess all vacuum test runs, and will be discussed in detail in the following section.

2. Force Measurement Procedure

This subsection will detail the step by step process used to take the optical displacement sensor data and quantify the magnitude of the impulsive force using the signal superposition approach. Figure 8 shows the same run from Figure 7 with some additional annotations to the data. There are two major sections of the optical displacement data that are tied to the impulsive calibration force (29 μN), and there is the center section that represents the response of the torsion pendulum system when the RF test article is energized with RF power. The raw data used to establish the "top" of the first calibration pulse, or left calibration pulse, includes the two highlighted sections of raw data that includes the data points with time ranges of 0 to 4.4 seconds, and 44.6 to 57.6 seconds. A line is fitted to the data, and the equation is shown above the highlighted data: $0.004615t + 1249.360$, where t is the variable time in sec, 0.004615 has units of μm/sec, and 1249.360 has units of μm.
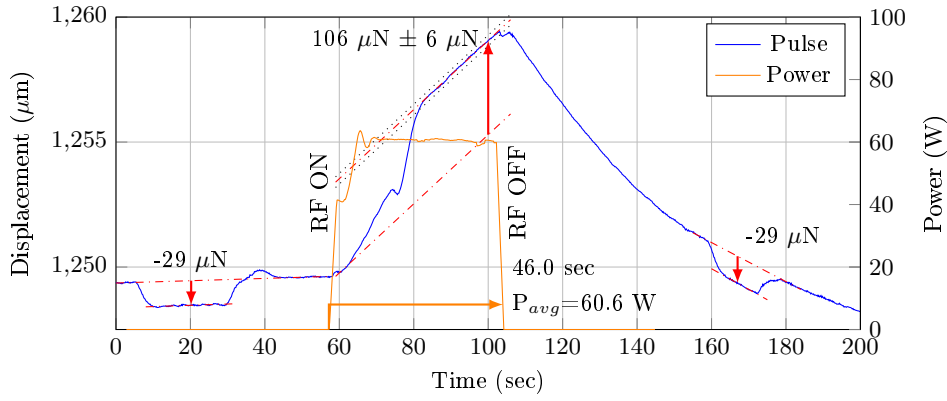
11

Fig. 7: Superposition of Signals: Test Article Run at 60 W in Vacuum.

The thrust rises slowly and peaks (break in slope) about 20 seconds after the RF power is initiated. Why isn't this instantaneous? As will be discussed in more detail at the end of the section on slope filtering, in order to run the test article in a fully integrated configuration, the torsion pendulum is operated in a highly loaded configuration which results in slower displacement rates for the torsion pendulum when an impulsive force is applied. Also note that in the case of this 60 W forward thrust test under vacuum conditions, the power signal also has some power fluctuations after the amplifier is activated (the power is also shown in the figure). This power oscillation corresponds to the small bump in displacement and the slope increases after the power oscillation is over.

The raw data used to establish the "bottom" of the first calibration pulse includes the highlighted section with a time range of 11.4 to 28.6 seconds. The equation of the line fitted to the data is shown below the highlighted data: $0.005095t + 1248.367$. The vertical separation between these two lines is determined at the middle of the first calibration pulse which is ~20.2 seconds on the time axis. The vertical separation between the top and the bottom of the first calibration pulse using the two fitted linear equations is 0.983 μm which corresponds with the calibration pulse magnitude of 29 μN.

The raw data used to establish the "top" of the second calibration pulse, or right calibration pulse, includes the two highlighted sections of raw data that includes the data points with time ranges of 155 to 158.6 seconds, and 178.8 to 184 seconds. A line is fitted to the data, and the equation is shown above the highlighted data: $-0.07825t + 1263.499$. The raw data used to establish the "bottom" of the first calibration pulse includes the highlighted section with a time range of 163.2

to 171.6 seconds. The equation of the line fitted to the data is shown below the highlighted data: $-0.0827t + 1263.163$. The vertical separation between these two lines is determined at the middle of the second calibration pulse which is $\sim$167 seconds on the time axis. The vertical separation between the top and the bottom of the second calibration pulse using the two fitted linear equations is 1.078 μm which corresponds with the calibration pulse magnitude of 29 μN.

The raw data used to establish the "top" if the impulsive force from the operation of the test article includes the highlighted section of raw data in the middle of the plot with a time range of 83.8 to 102.8 seconds. A line is fitted to the data and the equation is shown to the left of the highlighted data: $0.13826t + 1245.238$. The vertical axis intercept (1245.238) to this line is adjusted downward so that the line that represents the thermally shifted baseline will roughly intersect with the optical displacement curve where the RF power is turned on. This shifted baseline and its equation is shown on the plot: $0.13826t + 1241.468$. The vertical shift between the top of the impulsive force and the shifted baseline is 3.77 μm. The average vertical displacement of the two calibration pulses can be used to convert this vertical displacement number obtained from the shifted baseline to a force:

$$F = \frac{29\mu N}{\frac{0.983\mu m + 1.078\mu m}{2}} \times 3.77\mu m = 106\mu N \tag{1}$$

The fitted linear equations are used to generate the dash-dotted lines for the top and bottoms of the calibration pulses, the top of the impulsive force from the operation of the test article, and the shifted baseline in Figure 7, Figure 13, and Figure 16.

3. Slope Filtering: Alternate Approach

In the process of developing, applying, and reviewing the signal superposition approach, a suggestion was provided by reviewers to implement and evaluate slope filtering of the optical displacement data. If the important distinction is that there is a change in slope indicating the presence of both a thermal and impulsive signal, why not just take the derivative of the displacement signal and re-plot the curve only showing changes that are greater than a specified level? This has been done in Figure 9 using an aggressive slope filter level. Comparing the slope-filtered curve to the co-plotted raw displacement data, the two sections of the curve that are known thermal-only portions of the curve have been filtered to horizontal in the slope-filtered curve (see time ranges of
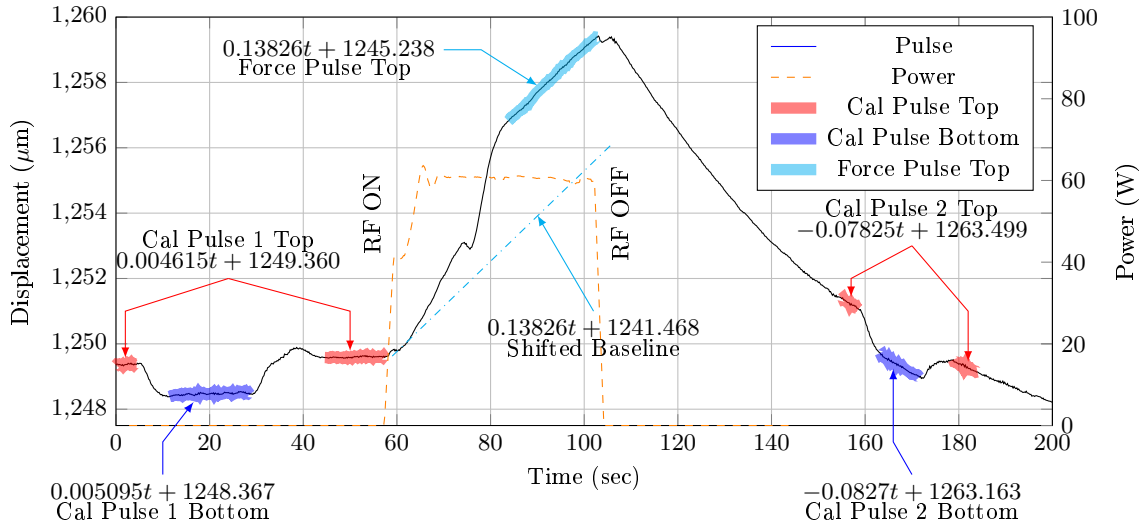
Fig. 8: Force Measurement Procedure Plot: The figure shows one of the 60W forward thrust runs with the data annotated to indicate the sections used to determine the calibration pulse characteristics, and the force pulse characteristics.

~80-100 seconds, and ~106-150 seconds). The characteristics of the second calibration curve after the test run are such that it has a large leading edge and small trailing edge to the pulse. This is a known impulsive signal that is present while there is also a significant thermal signal of same sense (negative-going). The characteristics of the curve while the RF power is applied to the test article are similar to this calibration pulse which may be an indication that there is an impulsive signal present with a same-sense thermal signal while the test article is energized. The critical filtered displacement values for the first and second calibration pulses and the curve when the RF power is applied are annotated on the figure, and these values can be used to calculate a force magnitude. Using the numbers shown to calculate the average displacements for the two calibration pulses and calculating the average force pulse displacement, the predicted force magnitude using this slope filtering technique is 124 μN.

One thing that was observed when implementing this approach was that the filter value necessary to "flatten" the sections of the displacement curve that are known to be thermal-only also resulted in the reduction in displacement magnitude for the leading calibration pulse, which is known to be a pure impulsive signal with no background thermal. A possible explanation for this is the fact that
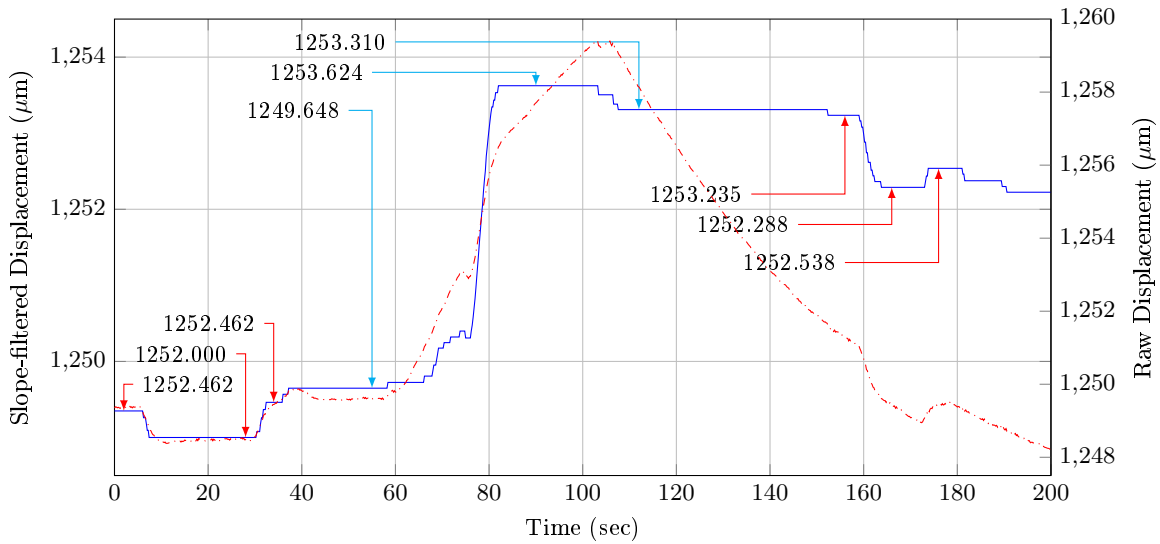
Fig. 9: Slope Filtering Plot with aggressive slope filter level.
The solid trace is the filtered data, and the dash-dotted trace is the raw unfiltered data. The critical displacement values for the leading calibration pulse, force pulse, and trailing calibration pulse are annotated on the plot. Using these numbers yields a predicted force magnitude of 124 μN.

the torsion pendulum is highly loaded with mass making the inertial response time to impulsive forces only slightly faster that the thermal response which means there will be some loss of impulsive data during aggressive slope filtering. The current implementation with an integrated test article and all necessary support electronics assembled into a single integral package requires a large amount of ballast to balance the pendulum arm leaving the torsion pendulum highly loaded. This highly loaded scenario has made the impulsive response time of the torsion pendulum considerably slower compared to the response times for previous tests in a "split configuration" mode.

In the split configuration mode, the amplifier and supporting electronics were on the opposite side of the pendulum from the test article which allowed this equipment to also serve as the ballast mass cutting the overall mass on the pendulum arm by a factor of two compared to the integrated approach. Figure 10 shows both ends of the pendulum bar for a split configuration with the test article on one end, and the support electronics on the other end serving as the ballast. The response of the pendulum in the split configuration mode to an impulsive signal was considerably faster by comparison to the current approach. The bottom pane of Figure 10 shows vacuum testing of the split configuration exciting the TM212 mode at 60 W. The calibration pulses have a magnitude of 29

μN. As discussed and can be seen in the data, the inertial response time for this split configuration is quicker than the integrated approach. Also, the thermal contribution for the split configuration is smaller in magnitude compared to the impulsive signal, which makes determination of the impulsive force magnitude an easier affair than the signal superposition approach that is used for the integrated test article implementation. The physical reason for this reduction in thermal contribution is likely due to the fact that the amplifier was on the back of the pendulum with the fins down and the amplifier on top, so thermal expansion of the aluminum heat sink only moves the amplifier mass up and does not drastically change the CG of the torsion pendulum arm in the horizontal plane. Future tests with the integrated test article approach will rotate the amplifier and heat sink such that it is in a similar orientation to this historical split configuration testing in an effort to reduce horizontal CG shift from thermal contributions.

The disadvantage to the split configuration which led to its abandonment was that performing forward and reverse thrust testing required complete disassembly and reassembly of the RF system when switching thrust directions which precluded the ability to establish a "frozen" RF tuning configuration, and is not compatible with the intention of performing force measurement testing at another location using another force measurement system. Also, as indicated in Section II B 1, tuning the thruster to generate optimal thrust is very difficult, and breaking configuration when switching from forward to reverse thrust was not practical.

4. Force Measurement Uncertainty

The contributors to the force measurement uncertainty are identified and quantified. The conversion from optical displacement to a force measurement is dependent upon a number of factors. The calibration force is provided by means of an electrostatic fin design (discussed earlier) that was calibrated offline using a Scientech SA210 precision weighing balance with a measurement uncertainty of +/-0.0001 g or +/-1 μN. The calibration campaign of the fin design evaluated the performance of the electrostatic combs through a range of fin engagement ranging from 10% engaged to 90% engaged. Based on this calibration campaign, the operational fin engagement range was established to be from 30% to 70% which provided roughly 3 mm of operational range, which
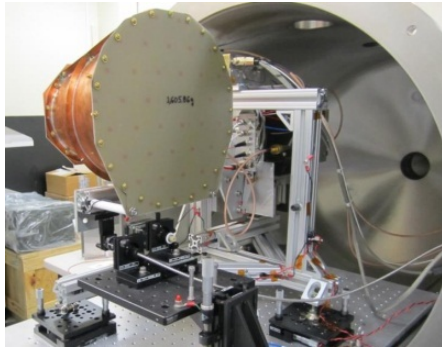
(a) Test Article
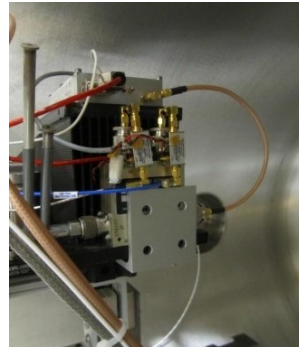
(b) Support Electronics (as ballast)
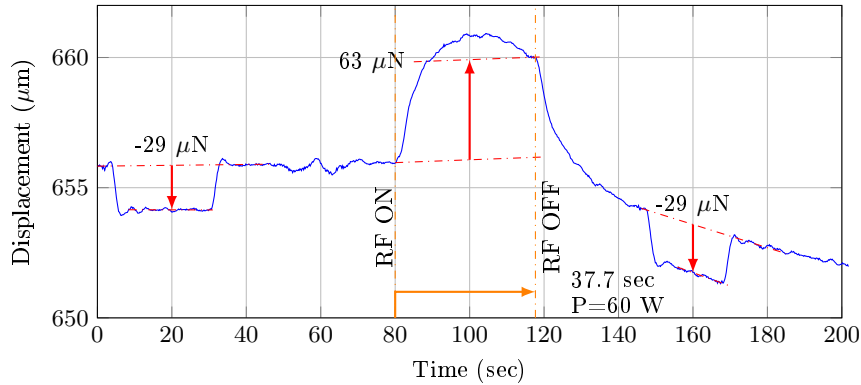
(c) 60W Forward Thrust Run at Vacuum for Split Configuration

Fig. 10: Split Configuration: The pictures show how the pendulum arm was loaded with the test article on one end, and the support electronics on the opposite end serving as ballast. The thrust trace illustrates the quicker rise times for the pendulum in response to an impulsive signal.

is well beyond what was needed for this campaign. The uncertainty in force measurement for this fin-engagement range can be as high as +/-2.2 μN when the fins are at the edges of the operational range. The calibration voltage is provided by a Fluke 343A DC Voltage Calibrator which has a voltage uncertainty of +/-0.004 V for a calibration voltage of 200 V which corresponds to a force uncertainty of +/-0.0005 μN. The optical displacement reading is provided by a Philtec muDMS-D63 displacement measurement system with a positional uncertainty of +/-0.01 μm when running in the far mode at 5 samples per second. Based on the magnitudes of the calibration forces used during the vacuum campaign, this corresponds to a force measurement uncertainty of +/-0.4 μN (worst case). The seismic contribution to positional uncertainty during vacuum runs was +/-0.05

μm which corresponds to a force measurement uncertainty of +/-2.2 μN (worst case). Seismic contributions can be larger in magnitude with a very low frequency on windy days due to waves in Galveston Bay and the Gulf of Mexico (see green run in Figure 12), but this is operationally controlled by not performing vacuum tests during windy conditions. The placement of the thermally compensated baseline discussed in the previous section may have some level of uncertainty due to establishing the intersection point of the shifted baseline and the start of the test. It should be noted that thermal baseline is assumed to be linear which fits well with observed behaviour. A conservative value of +/-0.2 μm is applied to this thermal uncertainty which corresponds to a force measurement uncertainty of +/-4.5 μN (worst case).

The root-sum-square of all of the measurement uncertainties yields a value of 5.6 which means the overall measurement uncertainty is +/-6 μN. Table 1 provides a tabulation of the measurement uncertainty contributions and the total measurement uncertainty.

Table 1: Measurement Uncertainty Tabulation

Source	Magnitude
SA210	±1 μN
Fin Calibration	±2.2 μN
Fluke 343A	±0.0005 μN
muDMS-D63	±0.4 μN
Seismic	±2.2 μN
Thermal	±4.5 μN
Total Error	±6 μN

5. Forward Thrust Overview

The tapered RF test article was mounted on the torsion pendulum as shown in Fig. 11. Forward thrust is defined as causing displacement to the left in the photo. Viewed from above, the torsion arm moves clockwise causing the mirror attached to the torsion arm to move away from the optical displacement sensor, which appears as an upward motion or positive displacement in the plots of displacement vs. time in Figs. 12 and 13. This displacement is also in the same direction as that
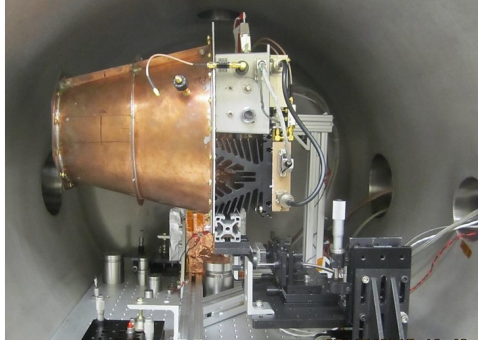
due to the CG shift from thermal effects.

Fig. 11: Forward Thrust Mounting Configuration (heat sink is black finned item between test article and amplifier).

A typical data run consists of: 1) a leading calibration pulse, typically either 200 volts or 300 volts equating to 29 μN or 66 μN respectively, that lasts for a few seconds and is released; 2) the RF system is energized for a period of time ranging from dozens of seconds to well over a minute; 3) an identical trailing calibration pulse. All data is saved digitally, and immediately after the run photographic evidence of the displays is also taken. During a run, the control and data acquisition system also records the power forward/reflected to/from the test article, and the RF amplifier temperature inside the vacuum chamber. Prior to testing in vacuum, an initial green run (a green run is defined here as a trial run to confirm proper tuning) is performed at ambient pressure (see Fig. 12). As discussed earlier in Section II C 1, the ambient pressure run shows considerably less thermal shift of the baseline and an almost entirely impulsive thrust pulse that exhibits similar mN/kW performance as the vacuum impulsive thrust.

The test article was run at 40, 60, and 80 W. Three runs were performed at each power setting for a total of nine vacuum tests in the forward thrust orientation. Once the system is at vacuum, the mixture ratio of impulsive signal to thermal baseline signal changes from the ambient in that there is more thermal baseline shift apparent in the data. Using the analysis techniques discussed in the Force Measurement Procedure section, the shifting baseline and impulsive signal can be decoupled, and a magnitude for the impulsive signal found. Figure 13 depicts thrust pulses representative of each power level used to collect statistical data. Table 2 shows a summary of the detected
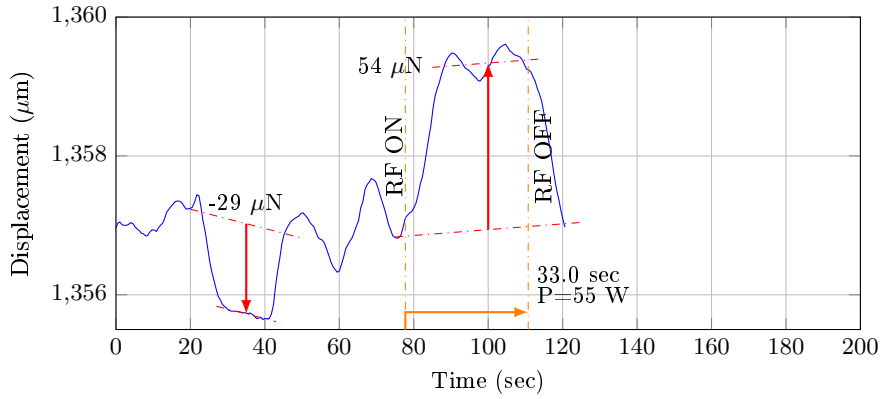
19

Fig. 12: Forward Thrust Green Run, Ambient Pressure Conditions. Error bars are not provided for green runs.

impulsive thrust from the forward thrust campaign conducted while the test article was under vacuum conditions ($<$ 8 microtorr).

Table 2: Forward Thrust Results in Vacuum Conditions (μN)

|	Power Band					
	40 W		60 W		80 W	
Run #	Power (W)	Force (μN)	Power (W)	Force (μN)	Power (W)	Force (μN)
Run 1	40.1	48±6	60.6	106±6	81.3	76±6
Run 2	40.8	30±6	59.7	91±6	83.5	119±6
Run 3	40.8	53±6	61.4	128±6	80.7	117±6

6. Reverse Thrust Overview

The tapered RF test article was mounted on the torsion pendulum as shown in Fig. 14. Reverse thrust is defined as causing displacement to the right in the photo. Viewed from above, the torsion arm moves counter-clockwise causing the mirror attached to the torsion arm to move towards the optical displacement sensor, which appears as a downward motion or negative displacement in the plots of displacement vs. time in Figs. 15 and 16. As the test article assembly was rotated by 180 degrees, this displacement is also in the same direction as that due to the CG shift from thermal effects.
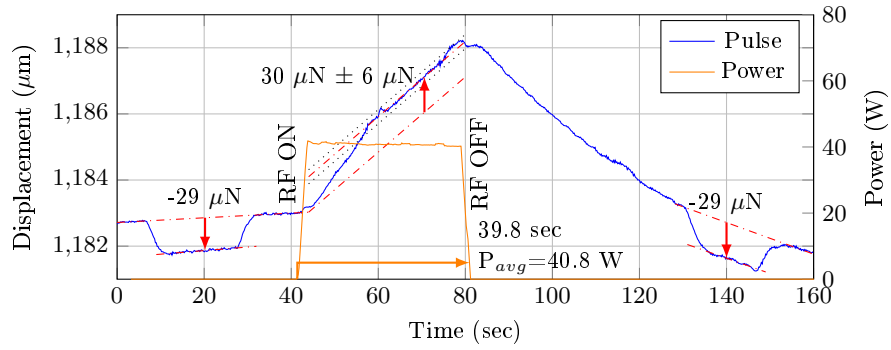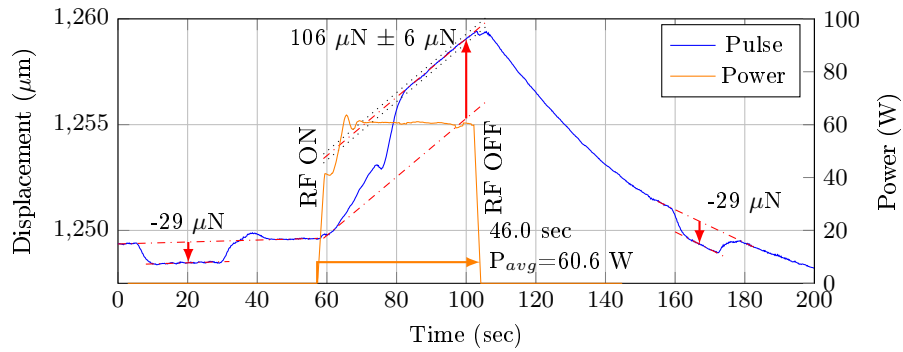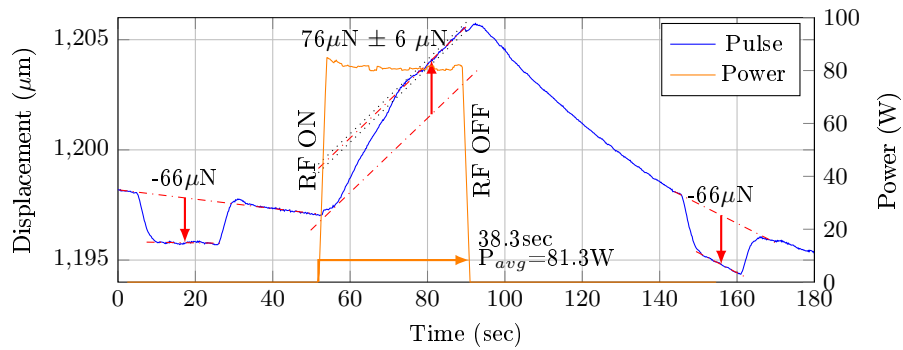
Fig. 13: Forward Thrust, at Vacuum, Representative Runs. Error bars (± 6 μN) are shown as black dotted lines.

The three figures show a run at 40 W (top), 60 W (middle), and 80 W (bottom). The power is co-plotted with the thrust trace. The calibration pulses are annotated based on the analysis of the optical displacement data. The signal superposition method is used to establish the magnitude of the impulsive thrust, and the results of the analysis are plotted on each figure.

Aside from pointing direction, the test procedure, power levels, data collection and initial green
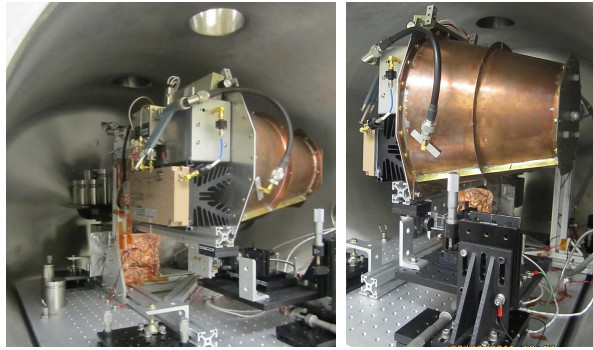
(a) View from left   (b) View from right

Fig. 14: Reverse Thrust Mounting Configuration.

run at atmosphere were performed identically to the forward thrust case. An additional event to highlight in this reverse thrust effort was that the system tuning was disturbed while transitioning between the 60 W and 80 W runs (the stub tuner position was moved inadvertently). This required a re-tuning of the system and a repeat of an ambient pressure green run. Figure 15 shows the preliminary ambient pressure run performed prior to reverse thrust vacuum testing, and the repeated ambient pressure run performed after re-tuning the system between the 60 W and 80 W testing.

The test article was run at 40, 60, and 80 W. Three runs were performed at each power setting for a total of nine tests in vacuum conditions in the reverse thrust orientation. Figure 16 depicts thrust pulses representative of each power level used to collect statistical data. Table 3 shows a summary of the detected impulsive thrust from the reverse thrust campaign conducted while the test article was under vacuum conditions (<8 microtorr).

Table 3: Reverse Thrust Results in Vacuum Conditions (μN)

|	Power Band					
	40 W		60 W		80 W	
Run #	Power (W)	Force (μN)	Power (W)	Force (μN)	Power (W)	Force (μN)
Run 1	40.9	40±6	60.2	43±6	83.2	74±6
Run 2	41.5	30±6	60.2	83±6	80	71±6
Run 3	41.4	30±6	59.1	67±6	80	69±6
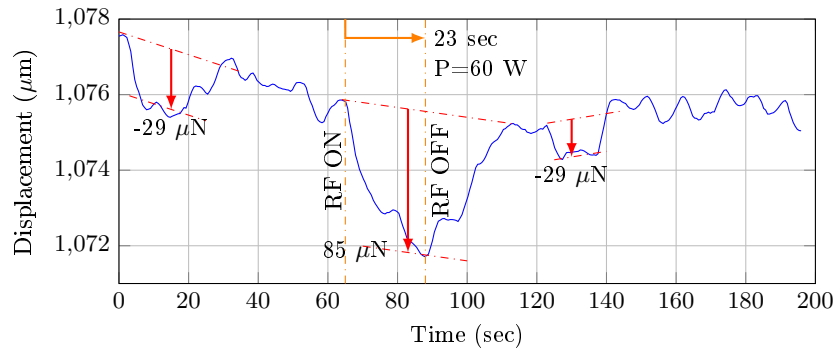
(a) Ambient Run #1
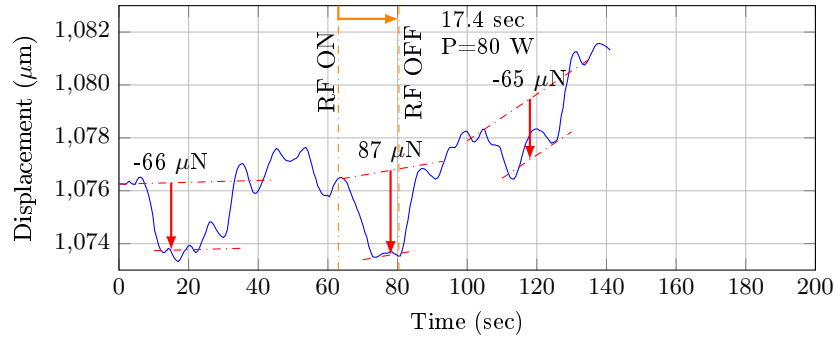
(b) Ambient Run #2

Fig. 15: Reverse Thrust Green Runs, Ambient Pressure Conditions. Error bars are not provided for green runs.

7. *Null Thrust Overview*

The tapered RF test article was mounted on the torsion pendulum as shown in Fig. 17. Null thrust parlance means that the test article is mounted to the torsion pendulum so that its major thrust axis is parallel to the torsion pendulum beam directed radially inward and unable to affect an impulsive thrust signal on the pendulum. The CG shift from thermal expansion causes a downward drift in the optical displacement sensor. This null thrust orientation allows the investigation to quantify any mundane impulsive thrust signals present associated with the operation of the integrated test article at full RF power. The null thrust testing campaign was undertaken at vacuum conditions, and there were three runs performed operating the integrated test article up to 80 W, or equivalent to the maximum power exercised during the forward and reverse thrust tests. Running at maximum power provides an upper bound on any impulsive systemic contribution to the detected
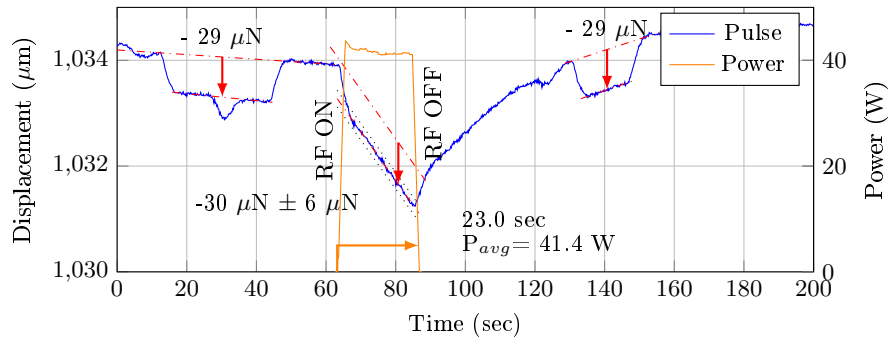
(a) 40 W
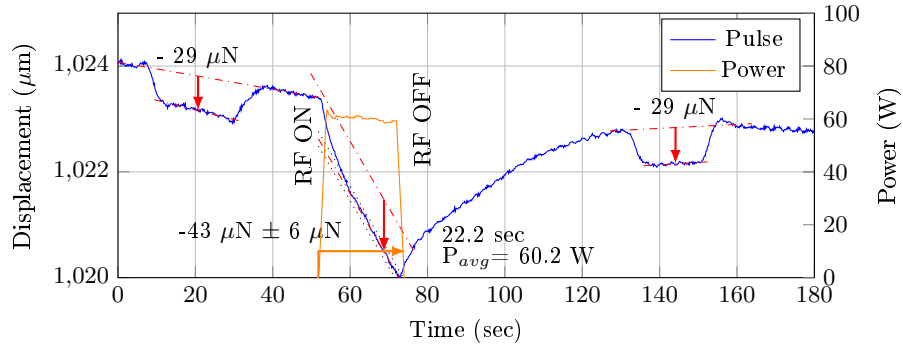
(b) 60 W
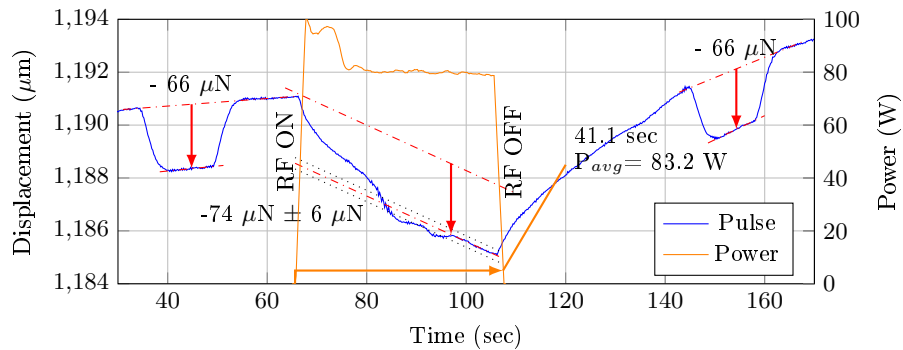
(c) 80 W

Fig. 16: Reverse Thrust, at Vacuum, Representative Runs. Error bars ($\pm$ 6 μN) are shown as black dotted lines.

The three figures show a run at 40 W (top), 60 W (middle), and 80 W (bottom). The power is co-plotted with the thrust trace. The calibration pulses are annotated based on the analysis of the optical displacement data. The signal superposition method is used to establish the magnitude of the impulsive thrust, and the results of the analysis are plotted on each figure.

thrust. Figure 18 depicts a representative null thrust test run at 80 W under vacuum conditions.
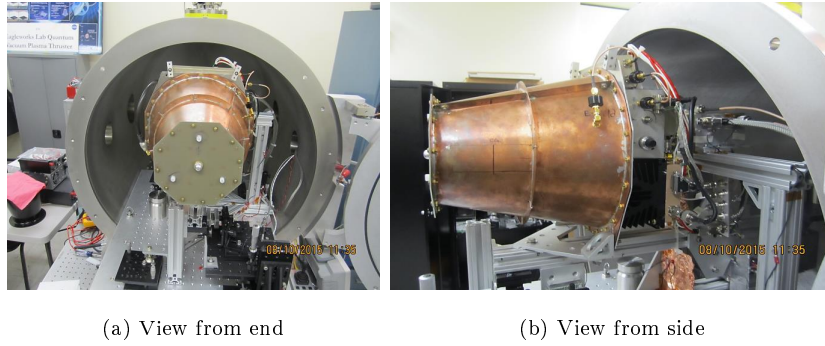
(a) View from end (b) View from side

Fig. 17: Null Thrust Mounting Configuration.

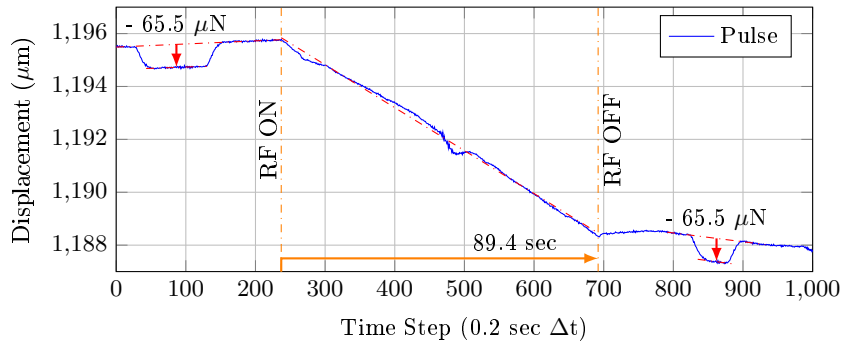The results from the null thrust testing show no impulsive element in the collected data, only the thermal signal.

Fig. 18: Null Thrust Test Run, at Vacuum, 80 W power: Shifting baseline due to thermal, no impulsive content.

8. *Error Sources*

A list of possible error sources is provided and discussed:

(a) *Air currents* possibly generating a false positive signal - the test article is tested in atmospheric conditions and under vacuum conditions. The impulsive thrust performance (mN/kW) was observed to be nearly the same.

(b) *RF interaction* with surrounding environment - potential for possible RF patch charging on walls of vacuum chamber interacting with the test article to cause displacement of torsion pendulum. Leaking RF fields are kept very low by ensuring RF connections are tight and confirmed by measuring

25

with an RF leakage meter (levels are kept below a cell phone RF leakage level). Any wall interaction would need to be a well-formed resonance coupling and because of the high frequency would be highly sensitive to geometry. Keeping the RF test article on resonance inside of the frustum volume requires a phase locked loop system to maintain resonance as the test article expands during operation, so it is not likely that the RF test article can establish and maintain an effective external RF resonance. Testing was performed with the torsion pendulum slid out of the vacuum chamber and an enclosure was built around the pendulum. While this generated similar force performance to that inside the chamber, the air currents made the quality of the signal poor. Although RF interaction with the chamber is not viewed by the investigation team as a likely false positive, a future way to totally eliminate any concerns would be to test in a larger vacuum chamber.

(c) *Magnetic interaction* - potential for false positive resulting from DC currents in power cables interacting during test article operation with ambient magnetic fields (e.g. local earth field, magnetic damper) to generate a torque displacement on the pendulum. All DC power cables are twisted pair or twisted shielded pair to minimize magnetic interaction. The test article is tested in a forward, reverse, and null thrust orientation, but DC power cable routing and orientation is the same for all three configurations (power cables come in from the top of the test article) meaning any false positives would be the same magnitude and polarity for all three tests. This was not observed during the test campaign.

(d) *Thermal* - thermal expansion and contraction of items mounted on the torsion pendulum will shift the CG of the pendulum and result in an offset displacement which can be a false positive. As was discussed in the section on signal superposition, any false positives from thermal will have a slower displacement response time on the torsion pendulum when compared to an impulsive thrust signal similar to the calibration pulse. Further, the test article is mounted to the torsion pendulum by means of two $^1/_4 - 20$ fasteners at the bottom of the entire assembly, so components of the test article assembly are free to thermally expand without constraint, resulting in a superposition of all thermal expansion sources being a curve that is uniformly logarithmic in nature with no discontinuities of slope. Said another way, since the test article is only constrained by two fasteners at the bottom, thermal expansion has no mechanical restraints relative to the CG of the torsion

26

pendulum. The integrated thermal signal for the system should be a uniform thermal signal with no discontinuities. Thus it is reasoned that any discontinuities in slope from the optical displacement sensor is a strong indicator of the presence of a non-thermal source of displacement. Although the performance of the impulsive signal under atmospheric and vacuum conditions was nearly the same, the magnitude of the thermal under vacuum conditions was much larger when compared to atmospheric conditions. To definitively rule out any residual concerns about thermal error sources, future test campaigns could employ a test apparatus capable of measuring small torques over much larger angular displacements. For example, a Cavendish balance approach properly designed to allow very large rotation angles such as, 90, 180, or even 360 degrees will not be susceptible to this type of thermal false positive.

(e) *Vibration* - false positives from vibration are not likely as vibration would not generate a steady state angular displacement of the torsion pendulum during operation. Contamination of displacement data from high amplitude vibration is mitigated by the 1.219 m x 2.438 m optical isolation table, and testing for the record is only performed on days where the ambient vibration levels still present during testing are of very low magnitudes compared to the displacements from test activities.

(f) *Electrostatic interaction* - potential for false positives from charging of moving components of torsion pendulum relative to stationary components of torsion pendulum and surrounding environment. All components of torsion pendulum and surrounding environment are held at a common reference ground by use of extensive grounding between components. This is confirmed with an ohm meter.

(g) *Outgassing* - potential for false positive from vaporization of surface molecules of dielectric insert or other non-metallic surfaces. During operation, the RF amplifier is the warmest component of the integrated test article. The RF amplifier is kept below 90 degrees F for hardware life preservation, and this temperature is monitored by the supporting lab equipment. Infrared imagery during operation of the test article shows that the larger end of the cone is the warmest portion of the RF resonance volume, but less than the amplifier. The dielectric is mounted on the smaller end of the tapered volume. Any outgassing that might occur from the dielectric insert would be vented from

27

the flat ends of the cone in an orthogonal, radial axisymmetric manner to the axis of the test article which would not be detected as a rectified force by the torsion pendulum. Additionally, force from outgassing being tied to thermal heating would likely have much slower rise and fall times when compared to the impulsive response from the calibration pulse. Said another way, outgassing would manifest as a slow increase in displacement (force) when the test article is active, and a similar slow decrease in displacement (force) back to zero after the test article is shut down and the system slowly cools down.

(h) *Photon rocket* - RF leakage from test article generating a net force due to photon emission. The performance of a photon rocket is several orders of magnitude lower than the observed thrust. Further, as noted in the above discussion on RF interaction, all leaking fields are managed closely to result in a high quality RF resonance system. This is not a viable source of the observed thrust.

(i) *Uncertainty in impulsive/thermal signal decoupling* - Some vacuum thrust traces are unambiguous, and decoupling impulsive from thermal is straightforward. In cases where the magnitude of drift gets very large compared to impulsive, the process is more challenging. One step to improve any given run is to minimize run time, as that keeps the drift magnitude lower. Another approach would be to reconfigure the integrated test article so that the RF heat sink is mounted in such a way that the thermal expansion is vertical as seen by the pendulum arm whereby minimizing thermal contamination. As noted earlier, to definitively rule out any residual concerns about thermal error sources, future test campaigns could employ a test apparatus capable of measuring small torques over much larger angular displacements.

9. Synopsis of Experimental Results

Figure 19 presents a collection of all the empirically collected data. The averaging of the forward and reverse thrust data is presented in the form of circles. A linear curve was fitted to the data and is shown with the corresponding fitted equation. The vacuum test data collected shows a consistent performance of 1.2 ± 0.1 mN/kW which is very close to the average impulsive performance measured in air (also 1.2 mN/kW). The error bars about the average data points represent a 2σ error. The error bars about the individual data points represents the force measurement uncertainty of $\pm$ 6
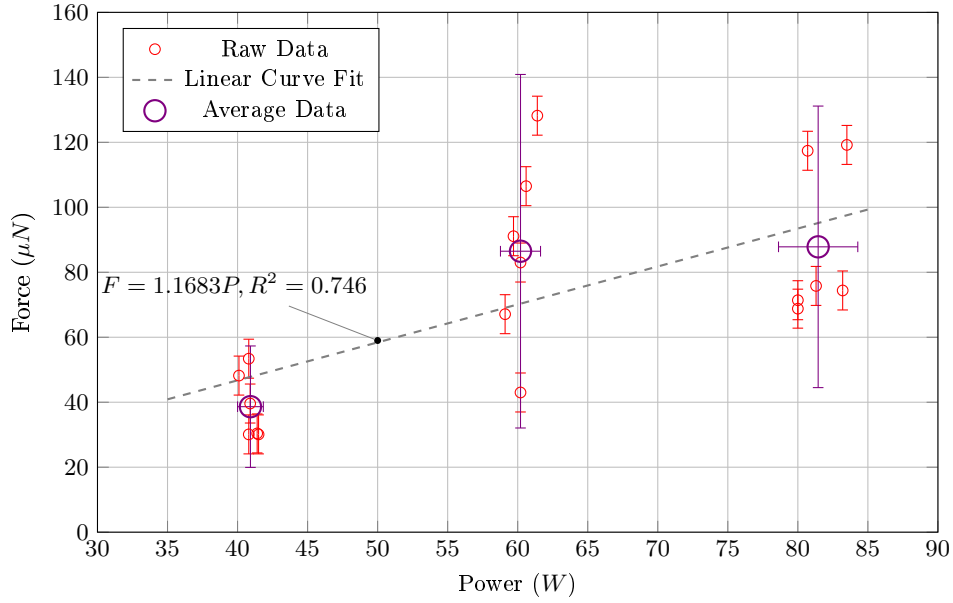
μN.

Fig. 19: Graph of Forward and Reverse Thrust Vacuum Testing.

10. Discussion

Prior to providing some qualitative thoughts on the proposed physics potentially at work in the tapered RF test articles, it will be useful to provide some brief background on the supporting physics lines of thought. In short, the supporting physics model used to derive a force based on operating conditions in the test article can be categorized as a non-local, hidden-variable theory, or pilot-wave theory for short.

Pilot wave theories are a family of realist interpretations of quantum mechanics that conjecture that the statistical nature of the formalism of quantum mechanics is due to an ignorance of an underlying more fundamental real dynamics, and that microscopic particles follow real trajectories over time just like larger classical bodies do. The first pilot wave theory was proposed by de Broglie in 1923 [4] where he proposed that a particle interacted with an accompanying guiding wave field, or pilot wave, and this interaction is responsible for guiding the particle along its trajectory orthogonal to the surfaces of constant phase. In 1926, Madelung [5] published a hydrodynamic model of quantum mechanics by recasting the linear Schrödinger equation into hydrodynamic form

29

where the Plank constant $\hbar$ is analogous to a surface tension σ in shallow-water hydrodynamics and vacuum fluctuations are the reason for quantum mechanics. In 1952, Bohm [6, 7] published a pilot wave theory where the guiding wave is equivalent to the solution of the Schrödinger equation and a particle's velocity is equivalent to the quantum velocity of probability. Soon after, the Bohmian mechanics line of thinking was extended by others to incorporate the effects of a stochastic subquantum realm and de Broglie augmented his initial pilot wave theory with this approach in 1964 [8] adopting the parlance "hidden thermodynamics". A family of models categorized as vacuum-based pilot wave theories or Stochastic Electrodynamics (SED) [9] further explore this idea in that the zero point field, electromagnetic vacuum fluctuations represent a natural source of stochasticity in the subquantum realm and provides classical explanations for the origin of the Planck constant, Casimir effect, ground state of hydrogen, and much more.

It should be noted that the pilot wave domain experienced an early setback when von Neumann [10] published an impossibility proof against the idea of any hidden-variable theory. This and other subsequent impossibility proofs were later discredited by Bell 30 years later in 1966 [11], and Bell goes on to say in the preface of his 1987 book [12] that the pilot wave eliminates the shifty boundary between wavy quantum states on the one hand, and Bohr's classical terms on the other - said simply there is a real quantum dynamics underlying the probabilistic nature of quantum mechanics.

While the idea of a pilot wave or realist interpretation of quantum mechanics is not the dominant view of physics today (which favors the Copenhagen Interpretation), it has seen a strong resurgence of interest over the last decade based on some experimental work pioneered by Couder and Fort [13]. Couder and Fort discovered that bouncing a millimeter sized droplet on a vibrating shallow fluid bath at just the right resonance frequency created a scenario where the bouncing droplet created a wave pattern on the shallow bath that also seemed to guide the droplet along its way. To Couder and Fort, this seemed very similar to the pilot wave concept just discussed, and in subsequent testing by Couder and others, this macroscopic classical system was able to exhibit characteristics thought to be restricted to the quantum realm. To date, this hydrodynamic pilot wave analog system has been able to duplicate the double slit experiment findings, tunneling, quantized orbits, and numerous other quantum phenomenon. Bush has put together two thorough review papers chronicling the

experimental work being done in this domain by numerous universities[14, 15].

In addition to these quantum analogs, there may already be direct evidence supportive of the pilot wave approach - specifically Bohmian trajectories may have been observed by two separate experiments working with photons [16, 17]. Reconsidering the double slit experiment with the pilot wave view, the photon goes through one slit, and the pilot wave goes through both slits. The resultant trajectory that photons follow are continuous real trajectories that are affected by the pilot wave's probabilistic interference pattern with itself as it undergoes constructive and destructive interference due to reflections from the slits.

In the approach used in the Quantum Vacuum Plasma Thruster (Q-thruster) supporting physics models, the Zero Point Field (ZPF) plays the role of the guiding wave in a similar manner to the vacuum based pilot wave theories. To be specific, the vacuum fluctuations (virtual fermions and virtual photons) serve as the dynamic medium that guides a real particle on its way. Two recent papers authored by members of this investigation team explored the scientific ramifications of this ZPF-based background medium. The first paper [18] considered the quantum vacuum at the cosmological scale in which a thought experiment applied to the Einstein tensor yielded an equation that related the gravitational constant to the quantity of vacuum energy in the universe implying that gravity may be viewed as an emergent phenomenon - a long wavelength consequence of the quantum vacuum. This viewpoint was scaled down to the atomic level to predict the density of the quantum vacuum in the presence of ordinary matter. This approach yielded a predicted value for the Bohr radius and electron mass with a direct dependency on dark energy. The corollary from this work pertinent to the q-thruster models is that the quantum vacuum is a dynamic medium and can potentially be modeled at the microscopic scale as an electron-positron plasma. The quantum vacuum around the hydrogen nucleus was considered in much more detail in the second paper[19]. Here, the energy density of the quantum vacuum was shown to theoretically have a $1/r^4$ dependency moving away from the hydrogen nucleus (or proton). This $1/r^4$ dependency was correlated to the Casimir force suggesting that the energy density in the quantum vacuum is dependent on geometric constraints and energy densities in electric/magnetic fields. This paper created a quasi-classical model of the hydrogen atom in COMSOL Multiphysics software (COMSOL is not an acronym)

that modeled the vacuum around the proton as an electron-positron plasma. These analysis results showed that the $n = 1$ to 7 energy levels of the hydrogen atom could be viewed as longitudinal resonant acoustic wave modes in the quantum vacuum. This suggests that the idea of treating the quantum vacuum as a dynamic medium capable of supporting oscillations may be valid. If a medium is capable of supporting acoustic oscillations, this means that the internal constituents are capable of interacting and exchanging momentum.

If the vacuum is indeed mutable and degradable as was explored, then it might be possible to do/extract work on/from the vacuum, and thereby be possible to push off of the quantum vacuum and preserve the Laws of Conservation of Energy and Conservation of Momentum. It is proposed that the tapered RF test article pushes off of quantum vacuum fluctuations, and the thruster generates a volumetric body force and moves in one direction while a wake is established in the quantum vacuum that moves in the other direction.

III.   Conclusions

A vacuum test campaign that utilized an updated integrated test article and optimized torsion pendulum layout has been completed. The test campaign consisted of a forward thrust element that included performing testing at ambient pressure to establish and confirm good tuning, and subsequent power scans at 40, 60, and 80 W with three thrust runs performed at each power setting for a total of nine runs at vacuum. The test campaign consisted of a reverse thrust element that mirrored the forward thrust element. The test campaign included a null thrust test effort of three tests performed at vacuum at 80 W to try and identify any mundane sources of impulsive thrust; none were identified. Thrust data from forward, reverse, and null suggests that the system is consistently performing at 1.2 ± 0.1 mN/kW which is very close to the average impulsive performance measured in air. A number of error sources were considered and discussed. While thermal shift was addressed to a degree with this test campaign, future testing efforts should seek to develop testing approaches that are immune to CG shifts from thermal expansion. As indicated in the error section, a modified Cavendish balance approach could be employed to definitively rule out thermal. Although this test campaign was not focused on optimizing performance and was more an exercise in existence proof,

it is still useful to put the observed thrust to power figure of 1.2 mN/kW in context. The current state of the art thrust to power for a Hall thruster is on the order of 60 mN/kW. This is an order of magnitude higher than the test article evaluated during the course of this vacuum campaign, however, for missions with very large delta-v requirements, having a propellant consumption rate of zero could offset the higher power requirements. The 1.2 mN/kW performance parameter is over two orders of magnitude higher than other forms of "zero-propellant" propulsion such as light sails, laser propulsion, and photon rockets having thrust to power levels in the 3.33-6.67 μN/kW (or 0.0033-0.0067 mN/kW) range.

Acknowledgments

References

[1] Brady, D., White, H., March, P., Lawrence, J., and Davies, F., "Anomalous Thrust Production from an RF Test Device Measured on a Low-Thrust Torsion Pendulum," *50th AIAA/ASME/SAE/ASEE Joint Propulsion Conference*, AIAA 2014-4029, AIAA, Jul. 2014. doi:10.2514/6.2014-4029

[2] Tajmar, M., and Fiedler, G., "Direct Thrust Measurements of an EMDrive and Evaluation of Possible Side-Effects," *51st AIAA/ASME/SAE/ASEE Joint Propulsion Conference*, AIAA 2015-4083, AIAA, Jul. 2015. doi:10.2514/6.2015-4083

[3] Yan, A., Appel, B., Gedrimas, J., "MilliNewton Thrust Stand Calibration Using Electrostatic Fins," *47th AIAA Aerospace Sciences Meeting including The New Horizons Forum and Aerospace Exposition*, AIAA, Jan. 2009. doi:10.2514/6.2009-212

[4] de Broglie, L., "Interpretation of quantum mechanics by the double solution theory," *Annales de la Fondation Louis de Broglie*, Vol. 12, No. 4, 1987, pp. 1-23.

[5] Madelung, E., "Quantentheorie in hydrodynamischer Form," *Zeitschrift für Physik A Hadrons and Nuclei*, Vol. 40, Issue 3, 1927, pp. 322-326. doi:10.1007/BF01400372

[6] Bohm, D., "A Suggested Interpretation of the Quantum Theory in Terms of "Hidden" Variables. I," *Phys. Rev.*, Vol. 85, Issue 2, 1952, pp.166-179. doi:10.1103/PhysRev.85.166

[7] Bohm, D., "A Suggested Interpretation of the Quantum Theory in Terms of "Hidden" Variables. II," *Phys. Rev.*, Vol. 85, Issue 2, 1952, pp.180-193. doi:10.1103/PhysRev.85.180

[8] de Broglie, L., "La thermodynamique ≪cachée≫ des particules," *Annales de l'I.H.P. Physique théorique*, Vol. 1, No. 1, 1964, pp.1-19.

[9] Boyer, T. H., "Any classical description of nature requires classical electromagnetic zero-point radiation," *American Journal of Physics*, Vol. 79, No. 11, 2011, pp. 1163-1167. doi:10.1119/1.3630939

[10] von Neumann, J., *Mathematische Grundlagen der Quantenmechanik* (Springer, Berlin 1932).

[11] Bell, J. S., "On the Problem of Hidden Variables in Quantum Mechanics," *Reviews of Modern Physics*, Vol. 38, Issue 3, 1966, pp.447-452. doi:10.1103/RevModPhys.38.447

[12] Bell, J. S., *Speakable and Unspeakable in Quantum Mechanics* (Cambridge Univ. Press, Cambridge, UK 1987).

[13] Couder, Y., Fort, E., "Single-Particle Diffraction and Interference at a Macroscopic Scale," *Physical Review Letters*, Vol. 97, Issue 15, 2006, pp.154101. doi:10.1103/PhysRevLett.97.154101

[14] Bush, J. W. M., "The new wave of pilot-wave theory," *Physics Today*, Vol. 68, 2015, pp. 47-53. doi:10.1063/PT.3.2882

[15] Bush, J. W. M., "Pilot-wave hydrodynamics," *Annual Review of Fluid Mechanics*, Vol. 47, 2015, pp. 269-292. doi:10.1146/annurev-fluid-010814-014506

[16] Kocsis, S., et. al., "Observing the Average Trajectories of Single Photons in a Two-Slit Interferometer," *Science*, Vol. 332, Issue 6034, 2011, pp.1170-1173. doi:10.1126/science.1202218

[17] Mahler, D. H., et. al., "Experimental nonlocal and surreal Bohmian trajectories," *Science Advances*, Vol. 2, Issue 2, 2016, e1501466. doi:10.1126/science.1501466

[18] White, H., "A Discussion on Characteristics of the Quantum Vacuum," *Physics Essays*, Vol. 28, No. 4, 2015.

[19] White, H., Vera, J., Bailey, P., March, P., Lawrence, T., Sylvester, A., and Brady, D., "Dynamics of the Vacuum and Casimir Analogs to the Hydrogen Atom," *Journal of Modern Physics*, Vol. 6, 2015, pp.1308-1320. doi: 10.4236/jmp.2015.69136